

# Open Research Online

---

The Open University's repository of research publications and other research outputs

## Validating a notch filter for detection of targets at sea with ALOS-PALSAR data: Tokyo Bay

### Journal Item

#### How to cite:

Marino, Armando; Sugimoto, Mitsunobu; Ouchi, Kazuo and Hajnsek, Irena (2014). Validating a notch filter for detection of targets at sea with ALOS-PALSAR data: Tokyo Bay. IEEE Journal of Selected Topics in Applied Earth Observation and Remote Sensing, 7(12) pp. 4907–4918.

For guidance on citations see [FAQs](#).

© 2013 IEEE

Version: Accepted Manuscript

Link(s) to article on publisher's website:

<http://dx.doi.org/doi:10.1109/JSTARS.2013.2273393>

---

Copyright and Moral Rights for the articles on this site are retained by the individual authors and/or other copyright owners. For more information on Open Research Online's data [policy](#) on reuse of materials please consult the policies page.

---

[oro.open.ac.uk](http://oro.open.ac.uk)

# Validating a notch filter for detection of targets at sea with ALOS-PALSAR data: Tokyo Bay

Armando Marino, *Member, IEEE*, Mitsunobu Sugimoto, Kazuo Ouchi, and  
Irena Hajnsek

## Abstract

The surveillance of maritime areas is a major topic for security aimed at fighting issues as illegal trafficking, illegal fishing, piracy, etc. In this context, Synthetic Aperture Radar (SAR) has proven to be particularly beneficial due to its all-weather and night time acquisition capabilities. Moreover, the recent generation of satellites can provide high quality images with high resolution and polarimetric capabilities. This paper is devoted to the validation of a recently developed ship detector, the Geometrical Perturbations Polarimetric Notch Filter (GP-PNF) exploiting L-band polarimetric data. The algorithm is able to isolate the return coming from the sea background and trigger a detection if a target with different polarimetric behavior is present. Moreover, the algorithm is adaptive and is able to account for changes of sea clutter both in polarimetry and intensity. In this work, the GP-PNF is tested and validated for the first time ever with L-band data, exploiting one ALOS-PALSAR quad-pol dataset acquired on the 9<sup>th</sup> of October 2008 in Tokyo Bay. One of the motivations of the analysis is also the attempt of testing the suitability of GP-PNF to be used with the new generations of L-band satellites (e.g. ALOS-2). The acquisitions are accompanied by a ground truth performed with a video survey.

Armando Marino is with the ETH Zurich, Institute of Environmental Engineering, Zurich, Switzerland (e-mail: marino@ifu.baug.ethz.ch). Mitsunobu Sugimoto is with National Defence Academy (NDA), Department of Information Science, School of Electrical and Computer Engineering, Japan. Kazuo Ouchi is with the Korean Institute of Ocean Science and Technology, Korea Ocean Satellite Center, Ansan, South Korea. Irena Hajnsek is with ETH Zurich, Institute of Environmental Engineering, Zurich, Switzerland and German Aerospace Centre (DLR), Wessling, Munich.

14 A comparison with two other detectors is presented, one exploiting a single polarimetric channel and the other  
15 considering quad-polarimetric data. Moreover, a test exploiting dual-polarimetric modes (HH/VV and HH/HV)  
16 is performed. The GP-PNF shows the capability to detect targets presenting pixel intensity smaller than the  
17 surrounding sea clutter in some polarimetric channels. Finally, the quad-polarimetric GP-PNF outperformed in  
18 some situations the other two detectors.

## 19 **Keywords**

20 Synthetic Aperture Radar, Radar Polarimetry, Ship detection, ALOS PALSAR, notch filter.

## 21 **I. INTRODUCTION**

22 This paper addresses ship detection with Polarimetric Synthetic Aperture Radar (PolSAR).  
23 Specifically a recent methodology proposed by the authors [1], [2], [3], [4] will be tested for  
24 the first time ever with L-band data (i.e. quad-polarimetric ALOS-PALSAR).

25 SAR provides an attractive combination of high resolution images acquired from space  
26 with relatively large swath width, night-time and all-weather capabilities [5], [6], [7], [8],  
27 [9], [10]. An introduction on SAR is outside the purposes of this paper and the authors  
28 redirect the readers to [11], [12], [13] for further details.

29 In SAR images, the main feature of a ship is a relatively large backscattering signal, which  
30 is usually brighter in comparison to the sea background. The strength of the signal from a  
31 vessel will be dependent on several factors, notably the size of the vessel and the material  
32 from which it is made, where generally, the presence of metallic reflectors (triangular and  
33 dihedral) will add to the overall brightness. For this reason, the intensity contrast was used  
34 as a feature to discriminate between targets and sea clutter. Several methodologies were  
35 proposed [6], [7], [8], [9], [10], [14], [15], [16], [17], [18], [19]. Most of these techniques  
36 set a statistical test between the intensities of target and clutter background.

37 It is increasingly common for SAR satellites to have the capability to acquire data em-  
 38 ploying different antenna polarization configurations [20]. In order to provide the maximum  
 39 amount of information the phase of the backscattering needs to be recorded in addition to the  
 40 amplitude of the separate polarimetric channels. Examples of satellites with such capabilities  
 41 are ALOS-PALSAR, TerraSAR-X and RADARSAT-2.

42 For instance, the use of the cross-polarized channel ( $S_{HV}$ ) instead than the co-polarized  
 43 ones ( $S_{HH}$  or  $S_{VV}$ ) in dual-polarimetric acquisitions may increase substantially the detec-  
 44 tion performance [2], [6], [14], [15], [16], [17], [18], [19], [21], [22], [23], [24], [25], [26],  
 45 [27]. This is because the sea has a small scattering contribution in the cross-polarized chan-  
 46 nel, therefore improving the Signal to Clutter Ratio (SCR). One way to combine several  
 47 polarimetric channels is considering them as independent measurements and set a statistical  
 48 test on them [21], [22]. These first techniques showed large improvements compared to the  
 49 single polarization detectors. From the analysis provided by Liu et al. [22] and shared by  
 50 other authors [28], it was shown that the quad-polarimetric mode provides the best detection  
 51 performance, followed by the dual co-polarization combination  $S_{HH}$  and  $S_{VV}$ .

52 A second type of polarimetric ship detectors is based on physical scattering properties  
 53 of targets and ships [2], [23], [24], [25], [28] (some of them exploited the difference in  
 54 coherence or degree of polarization shown by ships and sea clutter. The technique presented  
 55 in this paper, namely Geometrical Perturbation - Polarimetric Notch Filter (GP-PNF) was  
 56 developed in [1], [2], [3] and evaluates the differences in the polarimetric signature between  
 57 the sea and targets.

58 This paper is focused on testing the GP-PNF on ALOS-PALSAR data. L-band may be  
 59 particularly valuable for ship detection considering the backscattering from sea clutter is  
 60 expected to be lower compared to C- or X-band. Therefore, L-band may possibly bring some



61 advantage over rough sea conditions or thin sea-ice. In the specific context of this paper, a test  
 62 of the GP-PNF in L-band is necessary in order to verify the feasibility of using the algorithm  
 63 at this frequency. The detection rule is based on the concept that the polarimetric behavior  
 64 of targets and sea clutter remain separable. Considering the complexity of evaluating the  
 65 interactions between the transmitted polarized wave and the objects on the scene, it is not  
 66 trivial to state that vessels and sea will maintain a different polarimetric behavior that can  
 67 be detected by the GP-PNF as they were observed to do in other frequencies (i.e. C- and  
 68 X-band [1], [2], [3], [4]).

69 Additionally, the evaluation of the performance in L-band may be important in the context  
 70 of the next JAXA mission ALOS-2, in order to understand if the GP-PNF can be employed  
 71 with these data.

## 72 II. SHIP DETECTION WITH SAR POLARIMETRY

### 73 A. SAR polarimetry

74 The idea behind PolSAR is that the polarization of the electromagnetic (EM) wave can be  
 75 exploited to extract information regarding the identity of the observed targets [20], [29], [30],  
 76 [31], [32], [33]. Specifically, in order to characterize uniquely the behavior of a deterministic  
 77 target, four observations (quad-pol) have to be carried out. These can be arranged in the  
 78 *Scattering Matrix*:

$$[S] = \begin{bmatrix} S_{HH} & S_{HV} \\ S_{VH} & S_{VV} \end{bmatrix}, \quad (1)$$

79 where  $H$  stands for a horizontally linear polarized wave,  $V$  for linear vertical, and the re-  
 80 peated letter refers to transmitter-receiver. In the literature, a deterministic target that can be  
 81 characterized by only one (deterministic) scattering matrix is often defined as *single* [29].

82 An equivalent representation is by a scattering vector:

$$\underline{k} = \frac{1}{2} \text{Trace}([S]\Psi_2) = [k_1, k_2, k_3, k_4]^T, \quad (2)$$

83 where  $\text{Trace}(\cdot)$  is the sum of the diagonal elements of the matrix,  $T$  is for matrix transpose  
 84 and  $\Psi_2$  is a complete set of 2x2 basis matrices under a Hermitian inner product [29]. In  
 85 the case of a reciprocal medium and monostatic sensor (i.e. where the scattered radiation  
 86 is received at approximately the same position from which it was transmitted),  $\underline{k}$  is three  
 87 dimensional complex (i.e.  $\underline{k} \in \mathbb{C}^3$ ). Finally, it is possible to define the scattering mechanism  
 88 as a normalized vector  $\underline{\omega} = \underline{k}/|\underline{k}|$ .

89 However, for most target detection applications the target observed by a SAR system is not  
 90 a single idealized scattering target, but a combination of different targets which we refer to  
 91 as a *partial target* [29], [34], [35]. In the context of ship detection, the sea is sometimes  
 92 describable in terms of a single target (i.e. low entropy), however, especially when the  
 93 backscattering is very low and when the sea is rough the determinism of its behavior could  
 94 be removed. In order to characterize a partial target the second order statistics have to be  
 95 considered

$$[C] = \langle \underline{k} \underline{k}^{*T} \rangle, \quad (3)$$

96 where  $\langle \cdot \rangle$  is the finite averaging operator and  $*$  is for complex conjugate. The  $\Psi_2$  basis set  
 97 most commonly used is the Pauli (i.e.  $\underline{k} = [S_{HH} + S_{VV}, S_{HH} - S_{VV}, 2S_{HV}]^T$ ) since each  
 98 of the components is sensitive to a specific type of single target [29]. Specifically, ideally  
 99  $S_{HH} + S_{VV}$  represents a process that underwent an odd number of reflections (e.g. a single  
 100 reflecting surface or a trihedral corner reflector),  $S_{HH} - S_{VV}$  is an even bounce from a  
 101 dihedral with a horizontal corner and  $S_{HV}$  is a dihedral with a corner oriented at 45 degrees  
 102 with respect to the propagation plane (where 0 degrees stands for horizontal). In a maritime

context, it is expected that the  $S_{HH} + S_{VV}$  image will be more dominant over the sea surface, while the ship would have a strong component in  $S_{HH} - S_{VV}$  or  $S_{HV}$  (depending on ship orientation). The covariance matrix expressed with the Pauli basis is often referred to as Coherency matrix,  $[T]$ .

### B. Entropy detector

The Polarimetric Entropy can be calculated exploiting the Cloude-Pottier decomposition [32]. The latter is based on the diagonalization of the covariance or coherency matrix (as defined in eq. 3).  $[C]$  is an Hermitian semi-positive definite matrix. Therefore it can always be diagonalized. The eigenvalues are real positive and the eigenvectors form an ortho-normal basis for the space of the scattering vectors (a basis for which the three decomposed components are uncorrelated) [29]. The eigenvalues can be arranged to evaluate the entropy, which quantifies the possible dominance of one scattering mechanism over the others. The entropy is defined as:

$$H = - \sum_{i=1}^3 P_i \log_3(P_i) \quad (4)$$

$P_i$  are the probabilities of each eigenvalue and can be calculated as:

$$P_i = \frac{\lambda_i}{\lambda_1 + \lambda_2 + \lambda_3} \quad \forall i = 1, 2, 3 \quad (5)$$

where,  $\lambda_i$  are the eigenvalues.

As mentioned in the previous section, the entropy (or more generally other measures of depolarization) was proposed for ship detection [23]. The rationale behind this choice is that the sea has a rather deterministic polarimetric behavior that leads the pixels inside the averaging window to be rather coherent to each other. This returns a low value for  $H$ . On the other hand, the ships are targets presenting large heterogeneity among pixels composing

123 the Region of Interest (ROI). Therefore averaging them together will result in confused po-  
 124 larimetric information (i.e. large entropy). The detector is simply finalized with a threshold  
 125 on  $H$ :  $H > T_H$ . In the following the value used for the threshold is 0.5, since this showed to  
 126 provide the best detection performances. An automatic algorithm could be exploited, setting  
 127 the threshold fitting some statistical distribution of the sea clutter. In this comparison, the  
 128 supervised approach is preferred since it assures that the threshold is selected optimally (i.e.  
 129 not introducing errors due to a wrong estimation of the statistical distribution).

### 130 *C. CFAR with K-distributed intensity of $S_{HV}$*

131 This detector exploits single polarization data and considers a Constant False Alarm Rate  
 132 (CFAR) based on a K-distribution for the image intensity [6]. In this context the  $S_{HV}$  polar-  
 133 ization (i.e. cross polarization) channel was found to provide the best contrast between ships  
 134 and sea clutter for the incidence angle considered in this study (around 24 degrees) [6]. The  
 135 K-distribution is considered here because it was proved to model with adequate accuracy the  
 136 statistical behavior of texture for the sea clutter [6]. The selection of the threshold follows  
 137 a CFAR methodology where the probability of false alarm can be selected depending on the  
 138 specific applications. In this work, the value for the Probability of False Alarm ( $P_f$ ) was  
 139 selected as  $10^{-5}$  and the integrals were solved numerically. The algorithm exploited here  
 140 did not use local windows and the threshold was set selecting an area of 20 x 100 sea pixels  
 141 for each sector of 1000x5000 SLC pixels. This is to reduce the computational time of the  
 142 algorithm [6].

### III. POLARIMETRIC NOTCH FILTER

#### A. Mathematical Derivation

The ship detector presented in this paper shares the same general methodology of the Geometrical Perturbation - Partial Target Detector (GP-PTD). More details regarding the mathematical and physical justification of the algorithm can be found in [36], [37], [38], [4].

The first step is to construct a vector containing the second order statistics of the observed target. A feature partial scattering vector is introduced:

$$\begin{aligned} \underline{t} = \text{Trace}([C]\Psi_3) &= [t_1, t_2, t_3, t_4, t_5, t_6]^T = \\ &= [\langle |k_1|^2 \rangle, \langle |k_2|^2 \rangle, \langle |k_3|^2 \rangle, \langle k_1^{*T} k_2 \rangle, \langle k_1^{*T} k_3 \rangle, \langle k_2^{*T} k_3 \rangle]^T, \end{aligned} \quad (6)$$

where  $\Psi_3$  is a complete set of 6x6 basis matrices under a Hermitian inner product.  $\underline{t}$  lies in a subspace of  $\mathbb{C}^6$  representing all the physically feasible partial targets. The normalized version of  $\underline{t}$  can be considered:  $\hat{\underline{t}} = \underline{t}/\|\underline{t}\|$ . After a series of mathematical manipulations, the final expression of the PTD is:

$$\gamma_d = \frac{1}{\sqrt{1 + \text{RedR} \left( \frac{\underline{t}^{*T} \underline{t}}{|\underline{t}^{*T} \hat{\underline{t}}_T|^2} - 1 \right)}} > T_n. \quad (7)$$

where  $\hat{\underline{t}}_T$  represents the signature of the target to be detected (and can be any unitary vector in the space of the physically feasible targets),  $\underline{t}$  is the partial vector extracted from the scene (i.e. observables),  $T_n$  is the threshold and  $\text{RedR}$  is a detector parameter that can be set using a rationale based on the SCR [37].

The idea behind the GP-PNF is to build an algorithm that is able to identify any partial target which is different from the background clutter. In the case of ship detection, the

background is the sea. A conventional model for the electromagnetic scattering from the ocean's surface is the Bragg scattering model [29], [39]. Details on the Bragg model are not presented in this paper since the GP-PNF does not make any assumption regarding the specific behavior of the sea, as long as its backscattering is locally homogeneous.

Following the new vector formalism, the sea clutter can be completely characterized with a vector in a six dimensional complex space,  $\underline{t}_{sea}$ . On the other hand, the targets of interest can have a large variety of polarimetric signatures depending on orientation, material and structure of the vessel and a single vector would not be sufficient to identify any possible ship. The GP-PNF approach is to say that anything looking different from the sea background is a valuable target. In other words, this is equivalent to saying that the targets of interest lie in the complement orthogonal subset of the sea vector (five dimensional complex subset). Please note, in its formulation the proposed algorithm is quite general and can be used for detection of any target that is polarimetrically different from the background (even for land application, as long as the background has a stable polarimetric response). In case of sea observation, targets different from the sea would be ships, but also buoys, icebergs, wind turbines, small islands, etc.

Details regarding the mathematical derivation of the GP-PNF can be found in [1], [2], [3], [4], here only the final detector expression is presented for sake of brevity:

$$\gamma_n = \frac{1}{\sqrt{1 + \frac{RedR}{\underline{t}^{*T}\underline{t} - |\underline{t}^{*T}\hat{\underline{t}}_{sea}|^2}}} > T_n. \quad (8)$$

#### B. Dual-Polarimetric GP-PNF

Dual-polarimetric data are generally not sufficient to completely describe a partial target, however, in some instances the coherent acquisition of four polarizations is not feasible and

only two coherent acquisitions can be performed. The latter acquisition scheme generally takes name of dual-polarimetric mode [20], [29].

A dual-polarimetric scattering vector can be introduced as  $\underline{k}_d = [k_1, k_2]^T$ , with  $k_1$  and  $k_2$  being complex numbers (for instance  $S_{HH}$  and  $S_{VV}$ ). The covariance matrix can be estimated as:

$$[C_d] = \begin{bmatrix} \langle |k_1|^2 \rangle & \langle k_1^{*T} k_2 \rangle \\ \langle k_2^{*T} k_1 \rangle & \langle |k_2|^2 \rangle \end{bmatrix}. \quad (9)$$

Subsequently, a three dimensional partial feature vector can be built:  $\underline{t}_d = \text{Trace}([C_d]\Psi_2) = [\langle |k_1|^2 \rangle, \langle |k_2|^2 \rangle, \langle k_1^{*T} k_2 \rangle]^T$ . Finally, the dual-polarimetric detector is:

$$\gamma_{dn} = \frac{1}{\sqrt{1 + RedR \frac{1}{\underline{t}_d^{*T} \underline{t}_d - |\underline{t}_d^{*T} \hat{\underline{t}}_{dsea}|^2}}} > T_n, \quad (10)$$

where  $\hat{\underline{t}}_{dsea}$  is the normalized dual-polarimetric signature of the sea.

The mathematical derivations are presented in more details in [2], [3], [40].

### C. Parameter Selection

The GP-PNF has two parameters:  $T_n$  and  $RedR$ , which will determine the sensitivity of the detector. This means that one can be arbitrarily selected in its entire range of values (e.g.  $T_n \in ]0, 1[$  and  $RedR \in ]0, \infty[$ ) and the other is set based on the level of sensitivity required by the detector. The solution followed in this paper is to set the threshold to  $T_n = 0.9$  and choose the  $RedR$  based on the minimum intensity  $P_T^{min}$  of a target of interest in the subset complementary to the vector representing the sea:

$$RedR = (P_T^{min})^2 \left( \frac{1}{T_n^2} - 1 \right). \quad (11)$$

195 The square on  $P_T^{min}$  comes from the product  $\underline{t}^* \underline{t}$  which squares each of the components of  
 196 the covariance matrix.

197 The selection of a minimum target is needed to take into account some small heterogene-  
 198 ity in the sea and statistical errors in the estimations (due to finite number of samples). The  
 199 choice of the  $P_T^{min}$  depends on the vessel that the users are interested to detect. In case  
 200 that these are supposed to have large scattering (e.g. they are more than a hundred meters  
 201 long or they contain large metallic structures) a larger value will reject all the impurities in  
 202 the data, while if the vessels are expected to do not backscatter much (e.g. they are around  
 203 10 meters long or made of low reflecting materials) a smaller  $P_T^{min}$  should be chosen, but  
 204 some problems may arise with artifacts and ambiguities. This image defects are generated  
 205 by processing errors and may be interpreted as ships, since they appear as bright points in  
 206 the image [41]. Therefore, in such cases a good pre-processing (or post-processing) step for  
 207 cleaning ambiguities should be done besides the GP-PNF. In the dataset available, it is pos-  
 208 sible to observe only one strong azimuth ambiguity (as illustrated in the section concerning  
 209 false alarms analysis).

210 In this paper, the value chosen for the  $P_T^{min}$  is  $-15dB$  that corresponds to 0.029 in linear  
 211 scale. This value was chosen analyzing the curves of false alarms in Section V (the reader  
 212 is redirected to this section for further details). The choice of  $P_T^{min} = -15dB$  leads to  
 213  $RedR = 2 \cdot 10^{-4}$ . As a final remark it has to be said that the choice of  $P_T^{min}$  will be  
 214 clearly dependent on the specific sensor exploited and the typology of targets under analysis.  
 215 Parameters that can strongly influence the selection of  $P_T^{min}$  are frequency, resolution, noise  
 216 floor, dimension and material of vessels. The weather conditions clearly impact the detection  
 217 performance, however, as showed in [40] the GP-PNF is theoretically relatively stable against  
 218 weather conditions as long as the sea keeps on behaving as a locally homogeneous clutter.



219 Further work should be carried out to understand if sea clutter is locally homogeneous also  
 220 with particularly high sea states (this may also be function of the sensor resolution). In  
 221 other works of the authors, TerraSAR-X and RADARSAT-2 data were considered and the  
 222 values for  $P_T^{min}$  that were found to provide good results were respectively  $-7dB$  and  $-25dB$ .  
 223 Currently, work is ongoing on devising an algorithm able to set the threshold automatically  
 224 for any detection tasks (any frequency and resolution). In this context, some statistical test  
 225 may reveal promising, however, the derivation of the theoretical Probability Density Function  
 226 (pdf) of the GP-PNF output is not trivial and the test with some well-known distributions  
 227 may reveal very coarse. Additionally, some methodologies may consider iterative global  
 228 optimizations.

229 Regarding the selection of the filter null  $\hat{t}_{sea}$ , this is performed locally with a large mov-  
 230 ing window  $W_{tr}$ . Then the detection is performed within a smaller target window  $W$  (more  
 231 details about window sizes are provided in the validation section). A simple solution with  
 232 moving boxcar averaging (without guards) makes the detector particularly fast (1500x4000  
 233 pixels processed in few seconds with a regular desktop computer), and therefore feasible for  
 234 real time applications. Moreover, the use of guards was tested and it did not show significant  
 235 improvements. The reason of this is that the detection is performed on the base of the polari-  
 236 metric signature and not the intensity of the signal. Therefore, a contamination of  $W_{tr}$  will  
 237 not make the sea signature equal to the one of the target inside  $W$ , but just a combination of  
 238 of the different signatures of the extended vessel (if this is imaged in more than one pixel)  
 239 and the sea clutter [40].

#### IV. VALIDATION WITH ALOS-PALSAR DATA

##### A. Presentation of the datasets

The current GP-PNF validation experiment is performed with ALOS-PALSAR data. The algorithm was previously tested with different frequencies as C-band (RADARSAT-2) [2] and X-band (TerraSAR-X) [1]. This is the first time ever that the GP-PNF is tested with L-band data and it is interesting to understand if for this frequency polarimetry adds a contribution to enhance ship detection performance. L-band may represent an interesting scenario since the sea backscattering is expected to be relatively low at this frequency [39]. The dataset covers the Tokyo Bay area (Japan), which is renowned to have a large traffic of vessels. The acquisition was performed on the 9<sup>th</sup> of October 2008, (10:19 am local time). In this analysis Single Look Complex (SLC) data were considered. In order to reduce the speckle variation, a filtering was performed by the GP-PNF itself as described in the following. The resolution in ground range is 27 m, while in azimuth is 4.9 m. More details regarding the images are the following: the slant range resolution is 11.1 m, while the pixel spacing in slant range is 9.4 m (please note SAR images are over-sampled, therefore pixel spacing and resolution may be different); the pixel spacing in azimuth is 3.6 m. The incidence angle of these acquisitions is approximately 24 degrees.

The algorithm initially multi-looks the data 1x5 (range x azimuth) to make the pixel more squared on the ground. Subsequently, a target moving window of 5x5 pixels is exploited for the detection. Clearly, the samples are not all independent of each other and an Equivalent Number of Looks (ENL) can be calculated. In the following experiments, this is  $ENL = 50$ . In order to get a good estimation of the targets in the scene, as a general recommendation, the ENL should be kept higher than 25. Clearly, in case that the detection is focused on

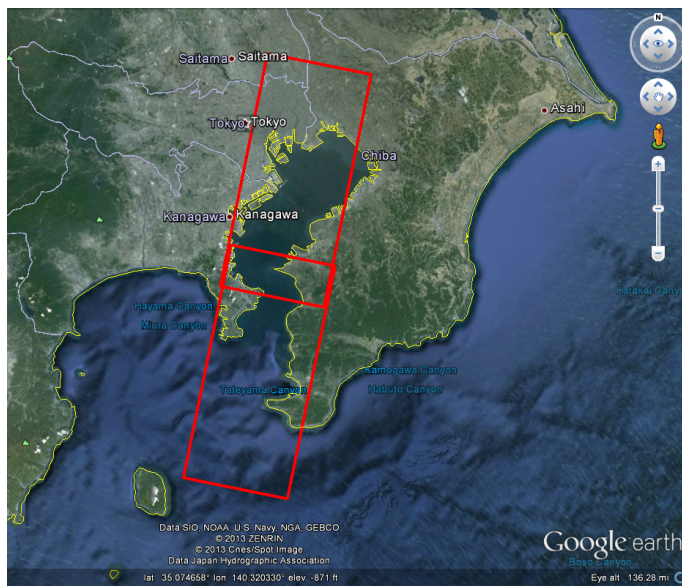
263 very small vessels, fewer pixels could be used. The big averaging window  $W_{tr}$  exploited to  
 264 extract the value of  $\hat{t}_{sea}$  is 20x20 pixels (after the initial multi-look) ending up with more  
 265 than 800 ENL.

266 During the acquisition a ground survey was carried out combining different instruments.  
 267 A video of vessels crossing a portion of the Bay was captured in cooperation with a X-band  
 268 ground-based radar. Both the video camera and radar were located on the top of the National  
 269 Defense Academy building (the west shore of the bay) at an altitude of approximately 100m  
 270 over the sea level [42]. Finally, Automatic Identification System (AIS) data were acquired,  
 271 but unfortunately only six vessels had an operating AIS transponder. Combining all this  
 272 information, the location of vessels was reconstructed.

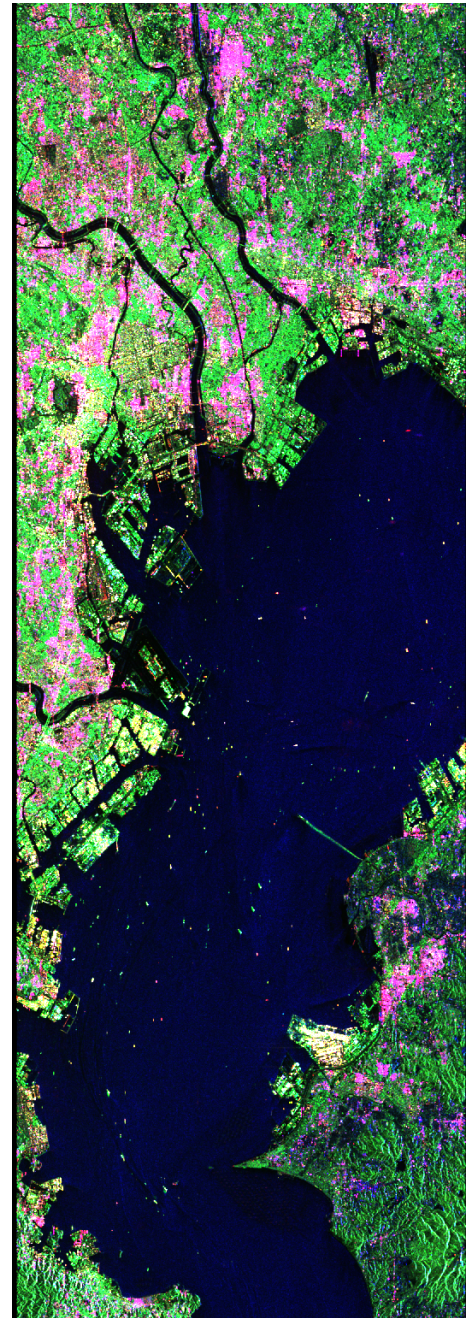
273 Regarding the sea state, the significant waveheight is 0.7m (three in Beaufort Scale) in  
 274 the direction  $190^\circ$  from North. The period is 1.8sec and the wind speed is 11.2m/s (strong  
 275 breeze: six in Beaufort Scale) in the direction  $20^\circ$ .

276 In order to have an idea of the geographical location of the test area, the aerial photo-  
 277 graph (taken from Google Earth) of Tokyo bay is presented in Figure 1, where the rectangles  
 278 represent the ALOS-PALSAR acquisition.

279 Before proceeding with the detection, it is interesting to have a preliminary look at the  
 280 polarimetric information visualizing the Pauli RGB composite image for the scene (Figure  
 281 1.b). Again, the RGB images are pre-processed multi-looking 1x5 the coherency matrix.  
 282 The Pauli basis is particularly valuable for the physical interpretation that can be attached to  
 283 its components. Specifically, the blue is sensitive to surface scattering, in this case the sea.  
 284 Looking at the image it is also clear the basic idea of the GP-PNF, since the sea background  
 285 appears polarimetrically homogeneous (i.e. it is blue everywhere except for spots of low  
 286 backscattering). Several targets are visible in the RGB image. The dataset is particularly



(a) Google Earth aerial photograph



(b) Pauli RGB

Fig. 1. ALOS-PALSAR quad-polarimetric dataset on Tokyo Bay ( $35.294451^{\circ}$ ,  $139.785816^{\circ}$ ),  $9^{th}$  of October 2008: (a) Google Earth aerial photograph with a rectangle indicating the ALOS-PALSAR acquisition; (b) Pauli RGB of the entire dataset, image size: 30x68km. Data provided by JAXA.

valuable since the scattering from the sea appears to be particularly high, with maximum values of the  $S_{VV} \sigma^0$  that are proximal to 0.7 (-1.5dB). Besides the weather conditions, this is due to the incidence angle that is relatively steep (24 degrees).

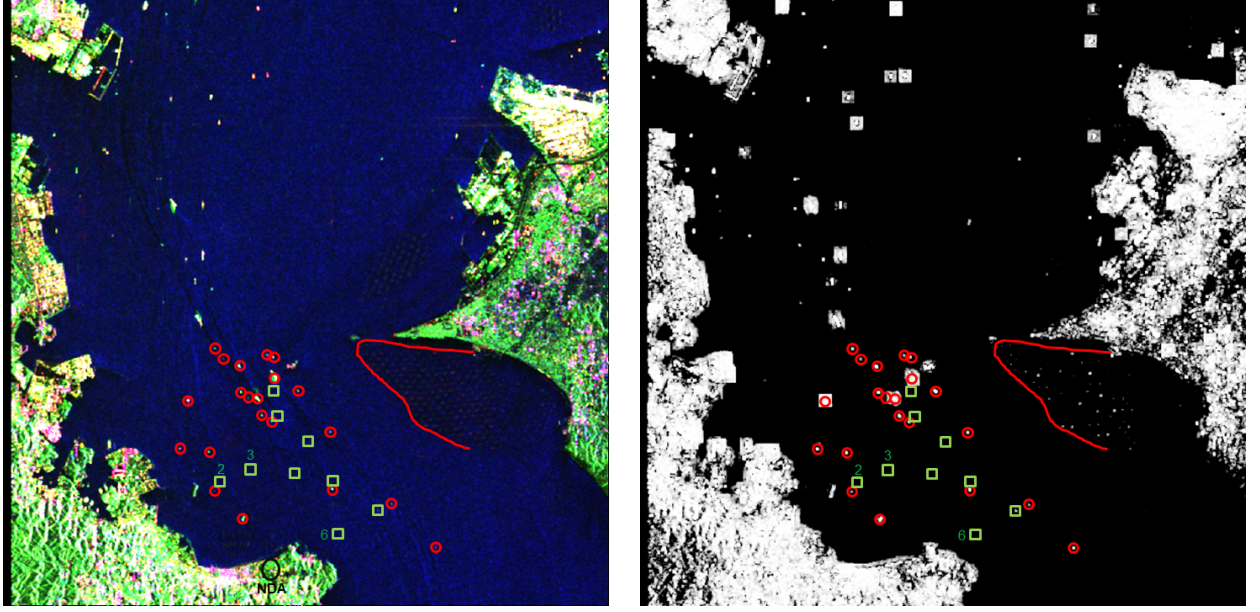
#### A.1 Detection over image crops: ground survey area

The RGB of the area of interest is presented in Figure 2.a with markers to identify features of interest. The red circles indicate vessels that were visible in the ground survey and can be identified in the RGB image. Green rectangles are vessels visible in the camera images but not in the RGB. This means that a visual inspection of the SAR images was not allowing detection. Some of the rectangles have a number indicating that this is not a single vessel but a cluster of small vessels very close each other. The area surrounded by the red line presents a seaweed farm (please note, inspection of Google Earth images showed that there is also another small seaweed farm more in the north and one close to NDA). In the following analysis, the same symbols are kept in order to compare the detection results with the visual inspection.

The GP-PNF detection mask with quad-pol is showed in Figure 2.b.

As it can be observed all the vessels in the red circles are detected by the GP-PNF quad-polarimetric detector. Additionally, one of the vessels that is not visible in the RGB (green rectangle) can now be detected, leading to 22 detected targets and 16 missing. If clusters of vessels are counted as one (since several small vessels may be in the same target window), the number of missing clusters would be 8. From the detection mask it is not possible to identify any false alarm. Finally, many of the seaweed platforms are identified, showing detection capabilities also for these wooden targets with low backscattering.

A comparison with dual-pol HH/VV and HH/HV is provided in Figure 3. An accurate



(a) RGB Pauli

(b) Quad-pol GP-PNF

Fig. 2. GP-PNF over the area provided of video survey (ALOS-PALSAR, JAXA): (a) RGB Pauli (b) Quad-pol GP-PNF with labels ( $P_T^{min} = -15dB$ ). Image size: 23x18km. ( $35.293664^\circ$ ,  $139.791927^\circ$ )

inspection of the detection masks shows that the HH/VV mode is identifying the same targets as for the quad-pol (22 vessels). The HH/VV detector used exactly the same parameters as the quad-polarimetric version. On the other hand, the HH/HV performance is slightly degraded with 20 vessels detected. In order to improve the detection capabilities of the HH/HV version the value of the  $P_T^{min}$  had to be lowered to 0.01 or -20dB. If the same value of the quad-pol version was used, only 14 vessels would be detected. Unfortunately, reducing the value of  $P_T^{min}$  may increase the false alarms as it can be observed in this test were three false alarms are visible (red stars). They appear as isolated points, therefore a morphological filter may be used to remove them. The authors leave this as future work.

The final test is performed comparing the GP-PNF with the entropy detector and the K-distributed CFAR over the  $S_{HV}$  intensity (Figure 4). The entropy detector is able to identify 21 vessels (one less than the GP-PNF). Specifically, the algorithm appears particularly suited



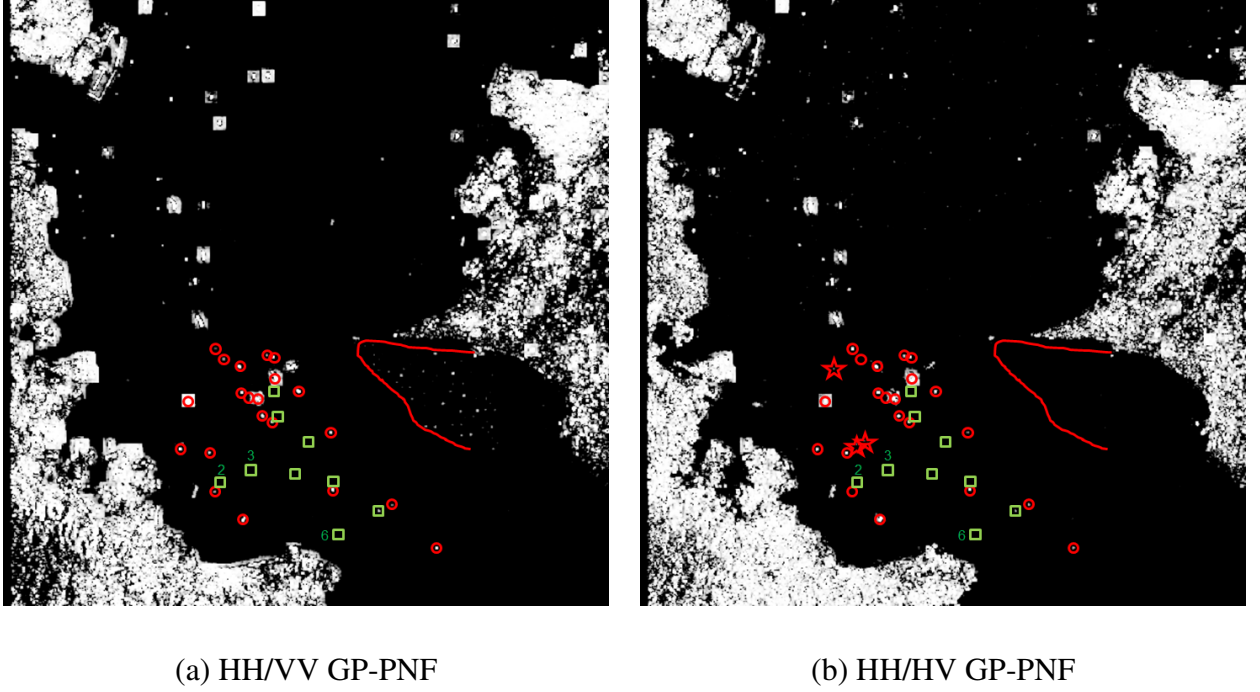


Fig. 3. GP-PNF over the area provided of video survey (ALOS-PALSAR, JAXA): (a) Dual-pol HH/VV GP-PNF ( $P_T^{min} = -15dB$ ); (b) Dual-pol HH/HV GP-PNF ( $P_T^{min} = -20dB$ ). Image size: 23x18km. (35.293664°, 139.791927°)

322 to identify the seaweed areas where almost all the platforms are detected [43]. Additionally,  
 323 also the other two farms are partially detected. Please note, a similar result for seaweed farms  
 324 detection is repeatable employing the quad-pol GP-PNF if the value of  $P_T^{min}$  is divided by  
 325 two or reduced of 3dB (i.e.  $P_T^{min} = -18dB$ ), but this introduces also two false alarms (the  
 326 detection mask is not showed for sake of brevity). Unfortunately, the entropy suffers from  
 327 false alarms, occurring when the backscattering level of the sea is low (some of these points  
 328 are indicated in the images with stars, but more than 20 isolated points could be counted).  
 329 This is because low backscattering leads to a scattering largely affected by noise that confuses  
 330 the polarimetric behavior increasing the entropy. Finally, this is supposed to be one of the  
 331 reasons (but not the only one) that contributes to the detection of the seaweed (laver) farms,  
 332 since these structures dampen the waves lowering the backscattering.

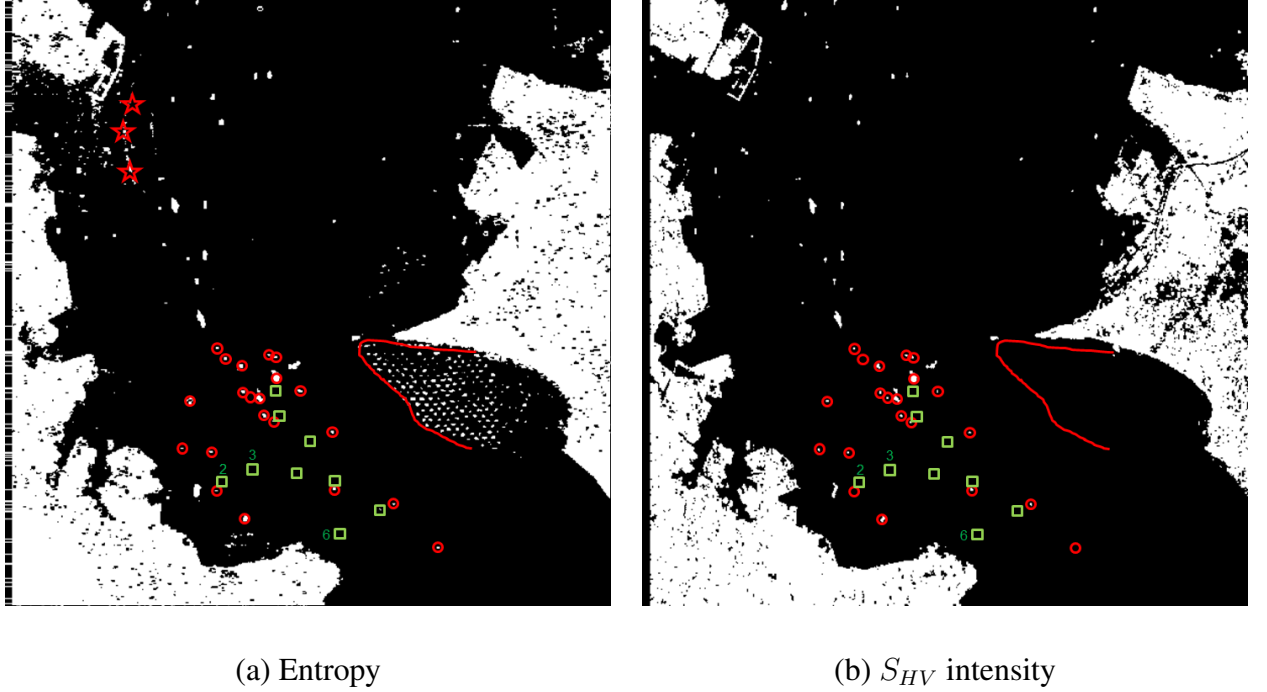


Fig. 4. Comparison with the entropy detector and the K-distributed  $S_{HV}$  intensity for the area with ground survey: (ALOS-PALSAR, JAXA): (a) Entropy with threshold 0.5 (b) CFAR with  $P_f = 10^{-5}$ . Image size: 23x18km. (35.293664°, 139.791927°)

333 The CFAR with the  $S_{HV}$  polarization presents a detection mask with lower performance.  
 334 Only 18 vessels are detected (four less than the quad-pol GP-PNF). Moreover, all the sea-  
 335 weed platforms are missing in the detection.

336 To summarize the results, Table I presents the number of vessels detected, missed and false  
 337 alarms for the area provided of video survey. The best detection performance on vessels is  
 338 showed by the GP-PNF quad-pol and HH/VV mode, with 22 over 38 vessels detected and  
 339 no false alarms. For the seaweed areas, the entropy appears to outperform the other algo-  
 340 rithms [43], but care has to be taken when using the entropy, since false alarms may occur  
 341 when the signal is low and seaweed farms are characterized by low backscattering (therefore  
 342 a pre-filtering of dark pixels would exclude the seaweed farms). The worst detection perfor-  
 343 mance is returned by the  $S_{HV}$  K-distributed CFAR. This is because the information of the



TABLE I

SUMMARY OF DETECTION RESULTS OVER THE VIDEO SURVEYED AREA AS PRESENTED IN THE

DETECTION MASKS			
Detector	Detections	Missing	False Alarms
GP-PNF (Quad-pol)	22	16(8)	0
GP-PNF (Dual HH/VV)	22	16(8)	0
GP-PNF (Dual HH/HV)	20	18(9)	3
CFAR ( $S_{HV}$ )	18	20(11)	0
Entropy	21	17(9)	> 20

co-polarizations is lost and they are particularly valuable to characterize the sea backscatter-  
ing.

Regarding the missing vessels we believe that higher resolution data may be beneficial  
to detect them. These vessels are not visible at all in the RGB image (not even after large  
zooming and inspecting the SLC of each polarimetric channel). They are supposed to be  
made of fiber-glass (without extensive metallic structures) and from the video survey they  
look particularly small (around or smaller than 10m).

## A.2 Detection over image crops: Tokyo Bay Aqua Line

The second image crop includes the Tokyo Bay Aqua Line (visible as a straight line on  
the East Coast). The RGB and quad-pol detection masks are presented in Figure 6 with  
some markers identifying features of interest. As for the previous case the backscattering  
from the sea is quite high (i.e.  $\sigma_{VV}^0 \approx -1.5dB$ ). The GP-PNF detects the points that  
could be easily attributed to vessels after a visual inspection of the RGB image. Please note,

the effect of enlarging the detection points is a consequence of the training window  $W_{tr}$ . When a bright target is analyzed the detection starts from the moment when the target enters the moving window  $W_{tr}$ . It is important to remark that this second area is not covered by ground survey, therefore only qualitative results can be provided. Nevertheless, the test is interesting to evaluate the stability of the choice for detector parameters and to compare different polarimetric modes.

The red ellipses identify areas where a line of targets is detected, however, looking at the RGB image no targets are visible there. In order to check for possible presence of targets, a Google Earth image of the area is provided in Figure 5. These detected points correspond to a mix of wooden water barrier approximately 20 m wide and 50 m long (i.e. flower shaped structures) and laver farms (i.e. dark stripes). In the SAR image they have a very weak backscattering which makes them impossible to detect using intensity, however the polarimetric information allows their separation from the sea background. A test of the quad-pol GP-PNF was performed using  $P_T^{min} = -18dB$  and not presented here for sake of brevity. The mask shows that with the lower threshold more targets are detectable, but since some of them are very weak in the RGB image it was not possible to state with some objectivity that they represent vessels.

The red triangle delineates an area that is suspected to be affected by image artifacts, specifically azimuth ambiguities from the nearby coast. Unfortunately, ground measurements are not provided to understand if this is an artifact or not. However, it is also important to notice that such artifacts are not distinguishable from genuine vessels and therefore they are detected by the algorithms. Fortunately, some pre-processing could be exploited to remove them before to run the detector.

The dual-pol modes HH/VV and HH/HV are presented in Figure 7. The two circles on

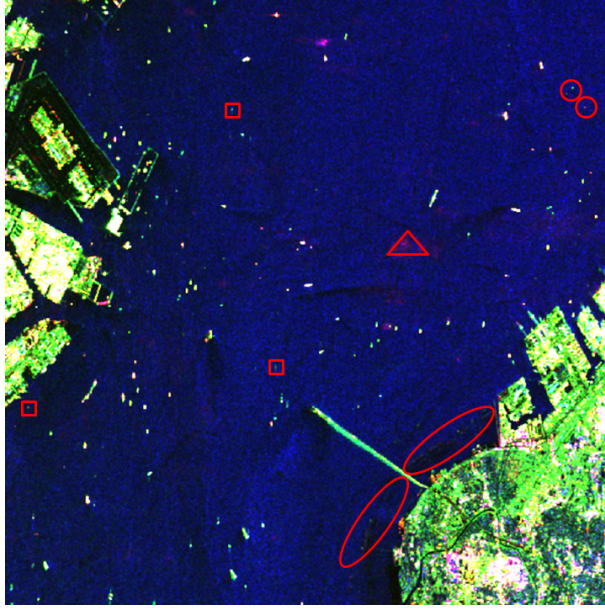


Fig. 5. Google Earth aerial photograph of some of the detected targets just beside Tokyo Bay Aqua Line.

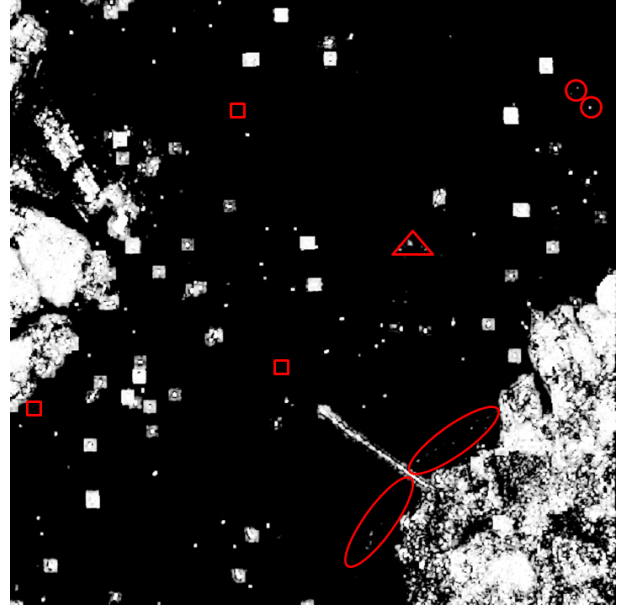
the up right corner present an interesting phenomenon: each of the dual-pol detectors can identify only one of the vessels, while the quad-pol detects both. Dual-polarimetry only considers partial information and when a target has no projection on the subspace observable by the two acquired channels then it will be missed in the detection mask.

The red diamonds indicate missing targets. It appears that the performance of HH/VV is still very close to the quad-pol mode, only for few exceptions (as the vessel in the red circle). HH/HV has several targets missing, among others, the small water barriers. Finally the red rectangles indicate points detected exclusively by the HH/HV mode. Looking at the RGB Pauli they appear as possible vessels, but of course they may just be false alarms. This is possible because the threshold used for the HH/HV is lower and therefore it allows the identification of vessels with a lower  $P_T^{min}$ . Interestingly, the quad-pol GP-PNF can detect these points if the threshold  $P_T^{min}$  is divided by two (i.e.  $P_T^{min} = -18dB$ ), but this introduces at least two apparent false alarms. For the HH/VV mode, reducing the value of  $P_T^{min}$  to  $-18dB$  allows only the detection of one of these three points.

The last test is with the other two detectors (Figure 8). As for the previous case, the entropy has good detection performance, especially for the small wooden barriers close to

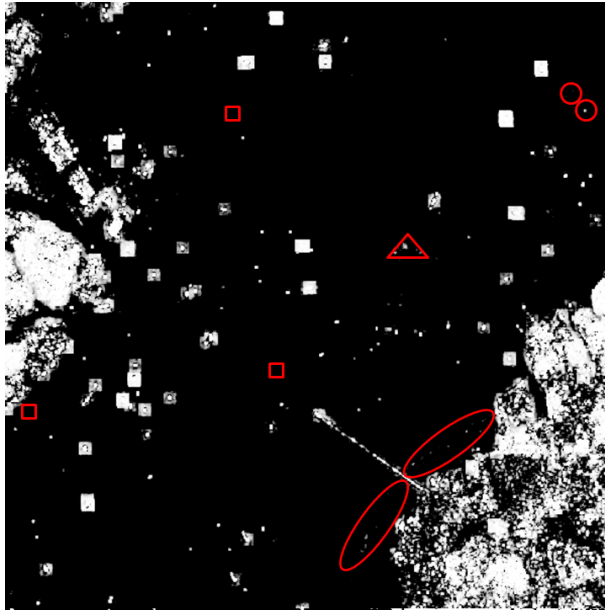


(a) Pauli RGB

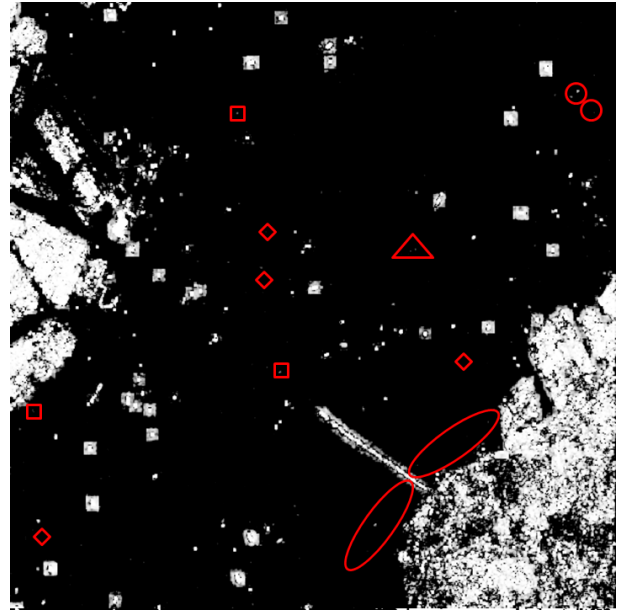


(b) Quad-pol GP-PNF

Fig. 6. GP-PNF over the area with Tokyo Bay Aqua Line (ALOS-PALSAR, JAXA): (a) RGB Pauli (b) Quad-pol GP-PNF ( $P_T^{min} = -15dB$ ). Image size: 23x18km. ( $35.520243^\circ, 139.850018^\circ$ )



(a) HH/VV



(b) HH/HV

Fig. 7. GP-PNF over the area with Tokyo Bay Aqua Line (ALOS-PALSAR, JAXA): (a) Dual-pol HH/VV GP-PNF ( $P_T^{min} = -15dB$ ); (b) Dual-pol HH/HV GP-PNF ( $P_T^{min} = -20dB$ ). Image size: 23x18km. ( $35.520243^\circ, 139.850018^\circ$ )

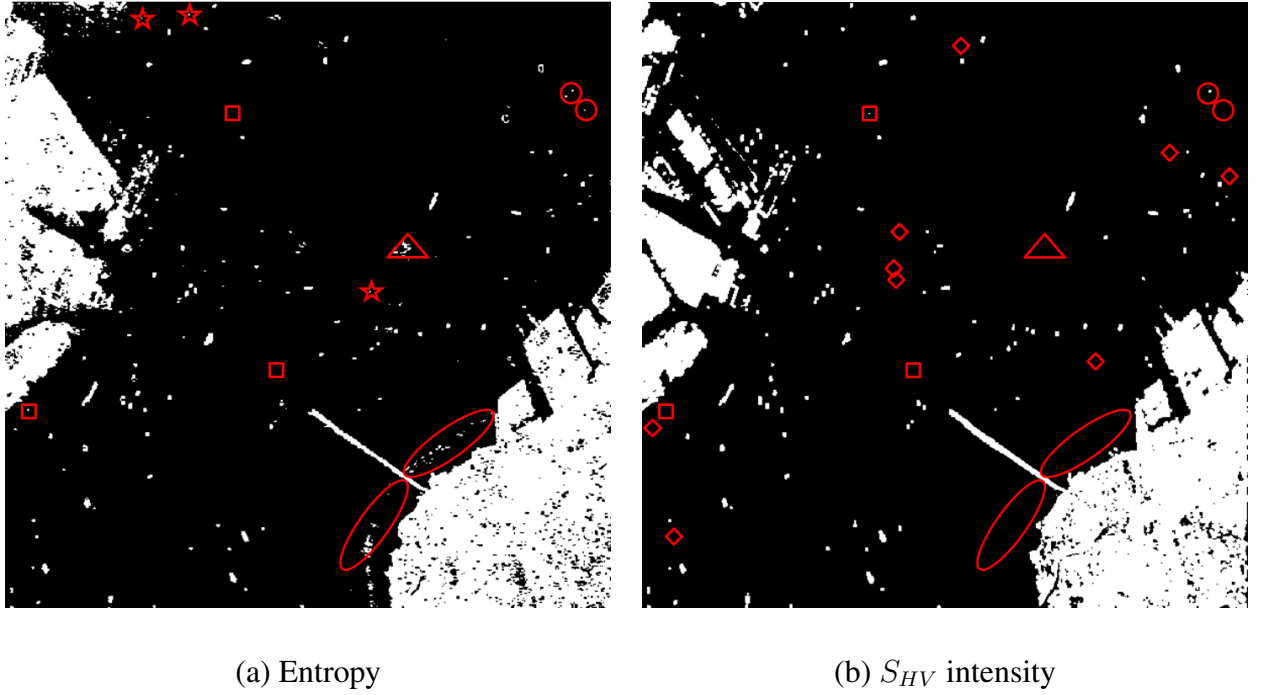


Fig. 8. Comparison with the entropy detector and the k distributed  $S_{HV}$  intensity for the area with ground survey: (ALOS-PALSAR, JAXA): (a) Entropy with threshold 0.5 (b) CFAR with  $P_f = 10^{-5}$ . Image size: 23x18km. ( $35.520243^\circ, 139.850018^\circ$ )

the Aqua Line. It is also possible to detect one of the targets in the red rectangles (the same detected by HH/VV with  $P_T^{min} = -18dB$ ). Unfortunately, the algorithm is again affected by false alarms where the backscattering is low (some of the points are indicated with red stars). The  $S_{HV}$  intensity detector is able to detect many targets that can be interpreted as vessels, but several are missing (indicated by nine red diamonds). The intensity detector is also able to identify one of the targets in the red rectangles.

## V. FALSE ALARMS AND ROC CURVES

### A. False alarms

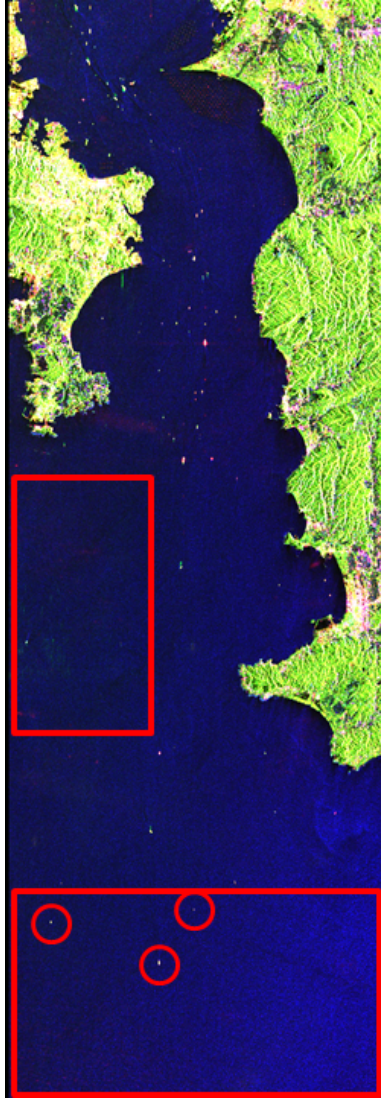
This final section is focused on investigating more quantitatively the false alarm rate on another area of the ALOS dataset(Figure 9.a). This water region is outside the entrance

of Tokyo Bay and therefore expected to have less presence of vessels (however a proper ground survey is not available). In the RGB Pauli, the two rectangles indicate the areas used to extract the statistics for false alarms (i.e. absence of targets). In the rectangle at the bottom of the image, three vessels are evident (zooming in, their wakes can be observed). In the following analysis, the pixels corresponding to these three vessels are removed. The uppermost rectangle presents an area where some bright pixels are visible. Zooming in the area, these pixels are distributed on a large area resembling an artifact (i.e. azimuth ambiguities). Nevertheless, we decided to include these pixels in order to provide a more general analysis.

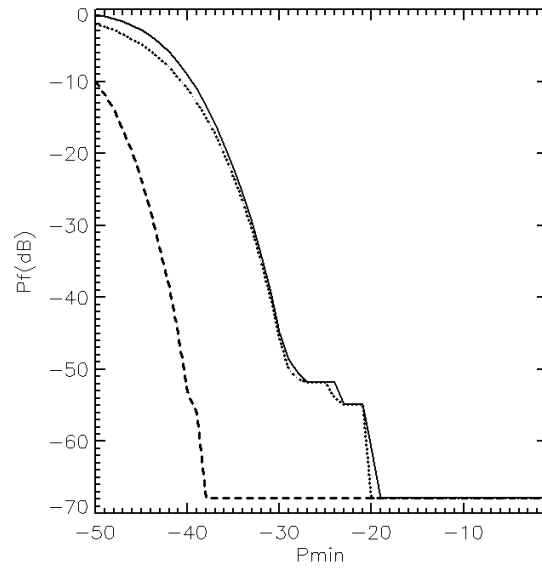
In this experiment, the probability of false alarm is calculated as the number of detected SLC pixels (before multi-look), over the total number of SLC pixels. Considering both the areas cover approximately 6.1 million pixels, the minimum  $P_f$  that can be estimated is equal to  $1.64 \cdot 10^{-7}$ . With the parameters exploited for the previous tests ( $P_T^{min} = -15dB$ ), the quad-pol GP-PNF shows no false alarms in the entire areas. However, to have a more exhaustive test, it is possible to plot the  $P_f$  as a function of  $P_T^{min}$  (expressed in dB). The results are showed in Figure 9. The GP-PNF quad-pol and HH/VV dual-pol exhibit a similar behavior, where the quad-pol shows a slightly higher  $P_f$ . The detection capability of quad-pol is higher than HH/VV dual-pol, therefore lower  $P_T^{min}$  are needed to obtain detection (in other words, the quad-pol mode collects more power coming from the target, compared to dual-pol modes). detections start appearing before in the quad-pol detector when  $P_T^{min}$  is varied. The HH/HV shows a lower detection capability, which in this context translates in better rejecting of false alarms.

In order to keep the false alarm rate very small (i.e. none of the 6.1 million pixels detected), the  $P_T^{min}$  should not be smaller than  $-20dB$  for quad-pol and HH/VV and  $-37dB$





(a) Pauli RGB



(b)  $P_f$  varying  $P_T^{min}$

Fig. 9. Analyzing the Probability of False Alarms: (a) Pauli RGB image of the area exploited (ALOS-PALSAR, JAXA); Red rectangles: areas used for the estimation of  $P_f$ ; Red circles: targets excluded by the analysis. Image size: 23x18km. ( $35.033164^\circ$ ,  $139.741118^\circ$ ); (b) Plot of  $P_f$  varying  $P_T^{min}$  for the GP-PNF: Solid line: quad-pol; Dotted line: HH/VV dual-pol; Dashed line: HH/HV dual-pol.

431 for HH/HV. Please note, the minimum value of  $P_T^{min}$  can be lower than the noise floor, since  
 432  $P_T$  is the power corresponding to a target in the complementary space of the background  
 433 clutter. As explained previously, thermal noise can be characterized with a unique  $\underline{t}$  vector  
 434 and it is expected to be locally homogeneous, therefore it is possible theoretically to reject it  
 435 with  $P_T^{min}$  much lower than the noise floor. False alarms are triggered as consequence of het-  
 436 erogeneity or estimation error due to the finite number of samples (as showed in [40]). The  
 437 latter fixes a boundary on the minimum value of  $P_T^{min}$ . As a final remark, it is important to  
 438 keep in mind that these results depend largely on the specific dataset (e.g. different weather  
 439 conditions or frequencies can lead to different plots).

## 440 *B. ROC curves*

### 441 B.1 Comparison of detectors

442 Once a meaningful analysis of  $P_f$  varying  $P_T^{min}$  is available this can be exploited in com-  
 443 bination with an analysis of  $P_d$  (over the validated test area) to plot the Receiver Operating  
 444 Characteristic (ROC) curve. The latter helps showing the detector performance indepen-  
 445 dently of the specific threshold selected. These curves also allow a fair comparison between  
 446 different detectors, since they are not based on the specific thresholds. In the previous sec-  
 447 tion, detection masks for the  $HV$  intensity and the entropy were illustrated. In order to  
 448 provide a larger validation another dual-pol detector is evaluated, which corresponds to set-  
 449 ting a threshold on the intensity of the  $HH - VV$  polarimetric channel (i.e. it may be referred  
 450 as a *dihedral* detector). The results are presented in Figure 10.a. The red lines are for the  
 451 GP-PNF, while the black ones for the other detectors.

452 The ROC curves present a dual behavior for values of  $P_d$  below and above 0.85:

- 453 1.  $P_d > 0.85$ : Three detectors show good performance with results fairly close each other:



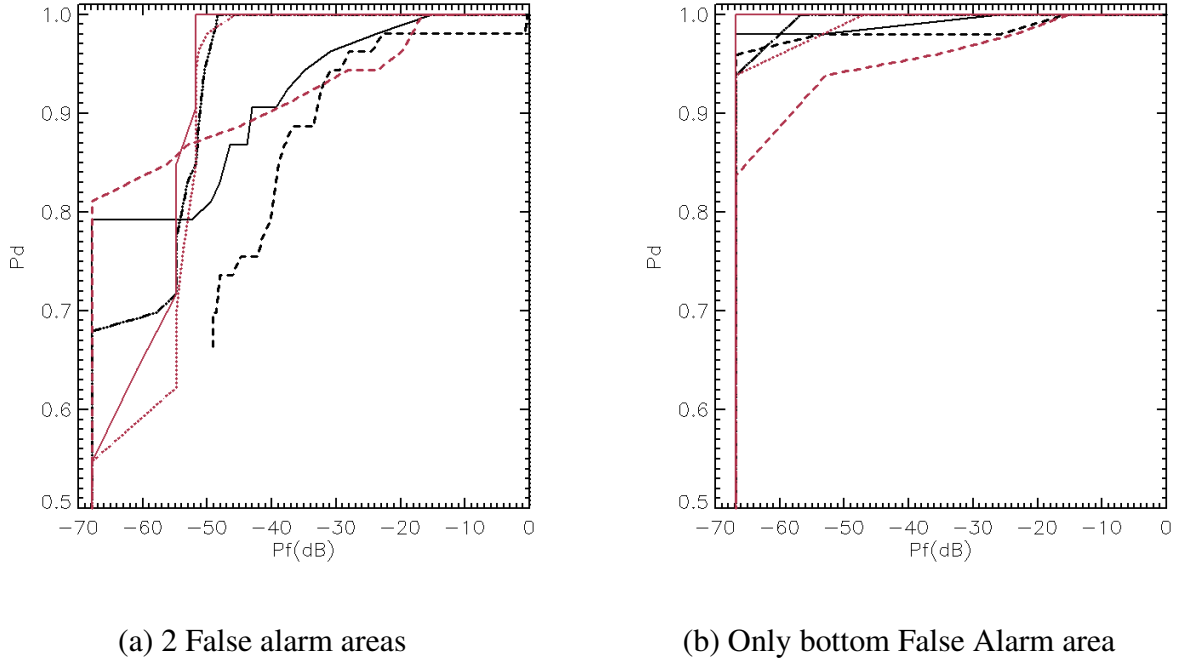


Fig. 10. ROC curves for GP-PNF (red) and other detectors (black). (a) Red solid line: quad-pol GP-PNF; Red dotted line: HH/VV GP-PNF; Red dashed line: HH/HV GP-PNF; Black solid line:  $HV$  intensity; Black dashed line:  $HH - VV$  intensity; Black dash-dot line: entropy.

the quad-pol GP-PNF, the HH/VV GP-PNF and the entropy. The curves suggest that in this dataset it is possible to have  $P_d \approx 1$  with  $P_f$  smaller than  $10^{-5}$ .

2.  $P_d < 0.85$ : It appears that the ROC curves of the previous three detectors have a drastic drop for  $P_f < 10^{-5}$ , while the HH/HV GP-PNF and the  $HV$  intensity appear to be quite unaffected by this drop. The reason is most likely due to the presence of artifacts (probably azimuth ambiguities from the nearby Tokyo) in the uppermost area (upper red rectangle in Figure 9.a). In actual fact, these artifacts are visible in the RGB image and they appear to affect the co-polarizations channels more than the cross-polarization one. To prove these, the uppermost area was removed from the analysis and the ROC was calculated again exploiting only the bottommost area. The resulting ROC are showed in Figure 10.b. The order of the curves (i.e. ranking between detector) is quite unmodified (at exception of the  $HV$  intensity,

which gains some position) however the problem with the drop (artifacts) disappears.

To conclude, the ROC curves show that on this dataset the quad-pol GP-PNF provides the best performance among the tested detectors, although the results obtained by the dual-pol HH/VV GP-PNF and the entropy detector are fairly close. The ROC's suggest that if the dataset is free from artifacts, the quad-pol GP-PNF can provide a  $P_f < 3 \cdot 10^{-7}$  with  $P_d = 1$ . However, in the more general case, where the dataset is expected to have some artifacts, the  $P_f$  should raise to  $10^{-5}$  in order to keep  $P_d = 1$ .

A last remark should be made regarding the entropy detector. In this experiment, it shows good behavior with respect to false alarms, but in the previous tests (closer to the city) it was possible to observe many false alarms in correspondence of ship wakes (where the signal is particularly low). As mentioned previously, the entropy should not be applied when the backscattering is low and therefore the detection performance showed by the ROC is only valid where this assumption is fulfilled (i.e. the backscattering is relatively high).

## B.2 Comparison of window dimensions

Finally, the ROC curves can be used to investigate the windows size that provides the best characteristic. Figure 11 shows the ROC when the target  $W$  and training windows  $W_{tr}$  are modified. The first plots consider a target window 5x5 (after the initial multi-looking), changing the dimension of the training window  $W_{tr}$ . While the second plots are for a target window 3x3. The solid lines are for  $W_{tr} = 20$  (as the one exploited in the previous experiments), the dotted lines are for  $W_{tr} = 30$  and the dashed lines are for  $W_{tr} = 10$ . The results are similar, however it can be noticed that if the background is not well characterized by a training window large enough, there may be a loss of detection performance. In these experiments, the combination that provides the best characteristics for  $P_d = 1$  is a target

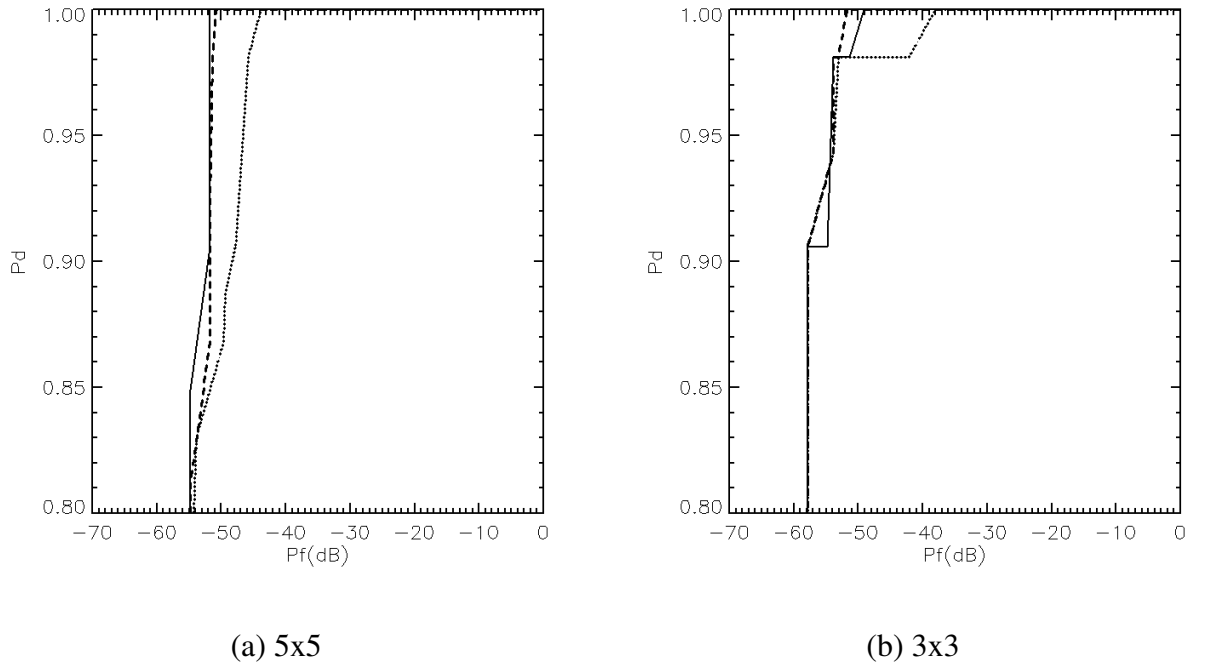


Fig. 11. ROC curves for GP-PNF fixing the target window to (a) 5x5 and (b) 3x3, varying the size of the training window. Solid line:  $W_{tr} = 20$ ; Dashed line:  $W_{tr} = 30$ ; Dotted line:  $W_{tr} = 10$ .

488 window 5x5 (after multi-looking) and training window 20x20 (this is the reason why these  
 489 values were employed in this work). However, looking at these curves also the choice 3x3  
 490 and training window 30x30 could be employed. Clearly, these results are strongly depen-  
 491 dent on the resolution of the sensor and the dimensions of vessels of interest. Therefore,  
 492 no definitive statement can be made and the windows' dimensions may change greatly if  
 493 another detection task (e.g. with another satellite sensor) is attempted.

#### 494 DISCUSSIONS

495 The aim of this section is to collect and discuss some of the results obtained in the  
 496 manuscript.

497 From the comparison of two dual-polarimetric modes with the GP-PNF, it can be ob-  
 498 served that HH/VV provides better performance than HH/HV (being almost as good as the

quad-pol version). Similar results were found comparing the different polarimetric modes exploiting other two ship detectors: the degree of polarization in Shirvany *et al.* [28] and the Generalized Likelihood Ratio in Liu *et.al* [22].

This may appear contradicting the fact that the best single channel for ship detection was demonstrated to be  $HV$  [23], [6]. An interpretation of these results is that the co-polarizations allow to characterize more precisely the sea polarimetric behavior and, therefore, to identify more accurately its complementary (target) subspace. Just as an example, exploiting only  $HH/HV$  it would not be possible to discriminate (from a polarimetric point of view) between Bragg scattering (often associated with the sea) and horizontal dihedral scattering (often associated with vessels).

Another remark could be made comparing the results presented in this paper with the ones recently obtained with RADARSAT-2 (where a ground survey was available) [44]. Exploiting RADARSAT-2 the GP-PNF was able to detect all the validated vessels in a dataset of four images (49/49). However, at this stage it is still not possible to come with some conclusive statement regarding the best frequency to exploit for ship detection, since the weather conditions, sensor resolution and typology of vessels are different in the dataset considered. Currently, work is in progress toward providing a fair comparison between different frequencies.

With the aim of testing the detector over a larger area and qualitatively compare the performance of different polarimetric modes, the GP-PNF was tested over the rest of the dataset. Please note, lacking of ground truth, it is not possible to provide any validation in this part of the dataset. The quad-pol gives the best detection performance narrowly followed by the  $HH/VV$  mode. However,  $HH/HV$  is able to detect at least two targets that can be retrieved with quad-pol (stressing the threshold) but not with  $HH/VV$ . This is a good indicator that all

523 the polarimetric information is important and even though the HH/VV mode could be a good  
524 substitute of quad-pol for ship detection, still there may be situations where some vessels are  
525 only detectable using quad-pol.

526 As a final remark, this paper wants to be a step in the process of thoroughly validating the  
527 GP-PNF for L-band. In order to have a definitive statement regarding the behavior of the  
528 detector (necessary for operational purposes) different sea states conditions and targets has  
529 to be considered, needing a larger amount of data.

## 530 CONCLUSIONS

531 In this paper the validation of a ship detector, the Geometrical Perturbations Polarimetric  
532 Notch Filter (GP-PNF) with ALOS-PALSAR data over the Tokyo Bay was presented. The  
533 GP-PNF bases its detection rule on the polarimetric differences between ships and sea back-  
534 ground. In details, a Null in the target polarimetric space is set in correspondence of the sea  
535 signature rejecting it and detecting the rest. This paper presented a test of the GP-PNF for  
536 the first time ever with L-band data.

537 The ALOS-PALSAR quad-polarimetric dataset was acquired over Tokyo Bay in Octo-  
538 ber 2008 presenting a very large amount of vessels of opportunity for testing the detector.  
539 Moreover, in one of the areas a video survey was carried out during the acquisition allow-  
540 ing quantitative analysis. 38 vessels were visible in the ground survey and of these 22 were  
541 detected by the quad-polarimetric GP-PNF. A visual inspection of the RGB image was per-  
542 formed and only 21 vessels were visible. The missing vessels were mainly small fiber-glass  
543 boats. Regarding false alarms, in the area observable by the camera no false alarms are  
544 identifiable in the quad-pol GP-PNF mask.

545 In order to test the feasibility of dual-polarimetry for ship detection, the GP-PNF was

546 applied to HH/VV and HH/HV data. As a general trend, the detection capability decreases  
 547 going from quad-pol to dual-pol HH/VV and finally to dual-pol HH/HV. This result was  
 548 already observed in other studies. An explanation is that the sea and ships are relatively well  
 549 characterized in the subspace observed by HH/VV, while using only one co-polarization a  
 550 large portion of the information may be lost.

551 In order to compare the detection mask in a larger context of ship detection, other two  
 552 detectors were considered. The first exploits quad-polarimetric data and estimates the po-  
 553 larimetric entropy, the second employs single polarization data and performs a test on the  
 554 intensity of the  $S_{HV}$  channel setting the threshold with a Constant False Alarm (using a  
 555 K-distribution). The results show that the entropy detector has a good detection capabil-  
 556 ity missing only one target more than the GP-PNF (21 instead than 22 detections), but it  
 557 is strongly affected by false alarms where the level of the backscattering is low. On the  
 558 other hand, the  $S_{HV}$  has no problems with false alarms but has a limited detection capability  
 559 compared to quad-polarimetric detectors (18 instead than 22 detections).

560 Finally, the scene presents areas with seaweed farms. Also due to the low backscattering  
 561 of the areas, the entropy provides very good detection and outperforms the GP-PNF, when  
 562 the ordinary threshold is used (the quad-pol GP-PNF misses some of the wooden platforms.  
 563 The  $S_{HV}$  intensity does not identify any wooden platform.

564 As a final analysis the false alarms are investigated in an area of the dataset where no  
 565 vessels are expected. The results are then used in cooperation with the validated detection  
 566 masks to provide Receiver Operating Characteristics (ROC) curves for comparing different  
 567 detectors. It appears that the quad-pol GP-PNF provides the best characteristics, followed  
 568 by the HH/VV GP-PNF and the entropy detector. Interestingly, the results suggest that it is  
 569 possible to have a probability of detection approximately equal to one with a Probability of

False Alarm smaller than  $10^{-5}$ .

## ACKNOWLEDGEMENTS

The authors would like to thank the Japanese Aerospace Exploration Agency (JAXA) for the kind provision of the ALOS-PALSAR data.

## REFERENCES

- [1] A. Marino and N. Walker, "Ship detection with quad polarimetric TerraSAR-X data: an adaptive notch filter," *Proc. on IGARSS'11*, 2011.
- [2] A. Marino, N. Walker, and I. H. Woodhouse, "Ship detection using SAR polarimetry. the development of a new algorithm designed to exploit new satellite SAR capabilities for maritime surveillance," *Proceedings on SEASAR, Frascati, Italy, January*, 2010.
- [3] A. Marino, N. Walker, and I. H. Woodhouse, "Ship detection with SAR data using a notch filter based on perturbation analysis," *Proceedings on IGARSS, Honolulu, Hawaii, July*, 2010.
- [4] A. Marino, "A notch filter for ship detection with polarimetric SAR data.," *IEEE Journal of Selected Topics in Applied Earth Observations and Remote Sensing*, vol. early access, 2013.
- [5] "Piracy and armed robbery against ships: Annual report," *ICC International Maritime Bureau, London, UK*, 2010.
- [6] D. J. Crisp, "The state-of-the-art in ship detection in synthetic aperture radar imagery," *Australian Government Department of Defence*, 2004.
- [7] K. Eldhuset, "An automatic ship and ship wake detection system for spaceborne SAR images in coastal regions.," *IEEE Transactions on Geoscience and Remote Sensing*, vol. 34, pp. 1010 – 1019, 1996.
- [8] P. W. Vachon, "Ship detection in synthetic aperture radar imagery.," *Proceedings OceanSAR, St. John s, NL, Canada*, 2006.
- [9] C.C. Wackerman, K.S. Friedman, W.G. Pichel, P. Clemente-Colon, and X. Li, "Automatic detection of ships in RADARSAT-1 SAR imagery," *Canadian Journal of Remote Sensing*, vol. 27, 2001.
- [10] G. Margarit, J. A. Barba Milanés, and A. Tabasco, "Operational ship monitoring system based on synthetic aperture radar processing," *Remote Sensing*, vol. 1(3), pp. 375–392, 2009.
- [11] G. Franceschetti and R. Lanari, *Synthetic Aperture Radar Processing*, CRC Press, 1999.
- [12] I.G. Cumming and F.H. Wong, *Digital Processing of Synthetic Aperture Radar Data: Algorithms and Implementations.*, Artech House, 2005.
- [13] C. Oliver and S. Quegan, *Understanding Synthetic Aperture Radar Images.*, SciTech Publishing, Inc, 2004.

- 599 [14] R.D. Chaney, M.C. Bud, and L.M. Novak, "On the performance of polarimetric target detection algorithms," *IEEE*  
600 *Aerospace and Electronics Systems Magazine*, vol. 5, pp. 10–15, 1990.
- 601 [15] L.M. Novak, M.C. Burl, and Irving W.W., "Optimal polarimetric processing for enhanced target detection," *IEEE*  
602 *Transactions on Aerospace and Electronic Systems*, vol. 29, pp. 234–244, 1993.
- 603 [16] L.M. Novak, M.B. Sechtin, and M.J. Cardullo, "Studies of target detection algorithms that use polarimetric radar  
604 data," *IEEE Transactions on Aerospace and Electronic Systems*, vol. 25, pp. 150–165, 1989.
- 605 [17] P.B. Chapple, D.C. Bertilone, R.S. Caprari, and G.N. Newsam, "Stochastic modelbased processing for detection of  
606 small targets in non gaussian natural imagery," *IEEE Transactions on Image Processing*, vol. 10, pp. 554 – 564, 2001.
- 607 [18] J. Gower and S. Skey, "Evaluation of RADARSAT ScanSAR for observing wind, slicks and fish-boats," *Canadian*  
608 *Journal of Remote Sensing*, vol. 26, pp. 484–493, 2000.
- 609 [19] J.S. Lee and I. Jurkevich, "Coastline detection and tracing in SAR images," *IEEE Transactions on Geoscience and*  
610 *Remote Sensing*, vol. 28, pp. 662–668, 1990.
- 611 [20] J. S. Lee and E. Pottier, *Polarimetric radar imaging: From basics to applications*, CRC Press, Taylor & Francis  
612 Group, 2009.
- 613 [21] D.J. Crisp and T. Keevers, "Comparison of ship detectors for polarimetric SAR imagery," *OCEANS 2010 IEEE -*  
614 *Sydney*, pp. 1–8, 2010.
- 615 [22] C. Liu, P. W. Vachon, and G. W. Geling, "Improved ship detection using polarimetric SAR data," *IGARSS Geoscience*  
616 *and Remote Sensing Symposium*, vol. 3, pp. 1800–1803,, 2004.
- 617 [23] R. Touzi, "On the use of polarimetric SAR data for ship detection," *IGARSS Geoscience and Remote Sensing*  
618 *Symposium*, vol. 2, pp. 812–814, 1999.
- 619 [24] M. Sugimoto, K. Ouchi, and Y. Nakamura, "Four-component scattering power decomposition algorithm with rotation  
620 of covariance matrix using ALOS-PALSAR polarimetric data," *Remote Sensing*, vol. 4(8), pp. 2199–2209, 2012.
- 621 [25] F. Nunziata, M. Migliaccio, and C.E. Brown, "Reflection symmetry for polarimetric observation of man-made metallic  
622 targets at sea," *IEEE Journal of Oceanic Engineering*, vol. 37(3), pp. 384–394, 2012.
- 623 [26] K. Ouchi, M. Iehara, K. Morimura, S. Kumano, and I. Takami, "Nonuniform azimuth image shift observed in the  
624 RADARSAT images of ships in motion," *IEEE Transaction on Geoscience and Remote Sensing*, vol. 30, 2002.
- 625 [27] S.-I. Hwang and K. Ouchi, "On a novel approach using MLCC and CFAR for the improvement of ship detection by  
626 synthetic aperture radar," *IEEE Geoscience and Remote Sensing Letters*, vol. 7, pp. 391 – 395, 2010.
- 627 [28] R. Shirvany, M. Chabert, and J.-Y. Tournet, "Ship and oil-spill detection using the degree of polarization in Linear  
628 and Hybrid/Compact Dual-Pol SAR," *IEEE Journal of Selected Topics in Applied Earth Observations and Remote*  
629 *Sensing*, 2012.
- 630 [29] S. R. Cloude, *Polarisation: Applications in Remote Sensing*, Oxford University Press, 2009.
- 631 [30] J.J. van Zyl, *Synthetic Aperture Radar Polarimetry*, John Wiley and Sons, 2011.



- 632 [31] W. M. Boerner, *Basics of Radar Polarimetry*, RTO SET Lecture Series, 2004.
- 633 [32] S. R. Cloude and E. Pottier, "A review of target decomposition theorems in radar polarimetry.," *IEEE Transaction on*  
634 *Geoscience and Remote Sensing*, vol. 34, pp. 498–518, 1996.
- 635 [33] J. R. Huynen, *Phenomenological theory of radar targets*, Ph.D. Delft: Technical University The Netherlands, 1970.
- 636 [34] G. A. Deschamps and P. Edward, "Poincare Sphere representation of partially polarized fields," *IEEE Transaction on*  
637 *Antennas and Propagation.*, vol. 21, pp. 474–478, 1973.
- 638 [35] Y. Dong and B. Forster, "Understanding of partial polarization in polarimetric SAR data.," *International Journal of*  
639 *Remote Sensing*, 17, vol. 17, pp. 2467–2475, 1996.
- 640 [36] A. Marino, *A New Target Detector Based on Geometrical Perturbation Filters for Polarimetric Synthetic Aperture*  
641 *Radar (POL-SAR)*, Springer-Verlag, 2012.
- 642 [37] A. Marino, S. R. Cloude, and I. H. Woodhouse, "Detecting depolarized targets using a new geometrical perturbation  
643 filter," *IEEE Transaction on Geoscience and Remote Sensing*, vol. In press, 2012.
- 644 [38] A. Marino, S. R. Cloude, and I. H. Woodhouse, "A polarimetric target detector using the Huynen Fork," *IEEE Trans.*  
645 *on Geos. & Rem. Sens.*, vol. 48, pp. 2357–2366, 2010.
- 646 [39] C. Elachi and J. van Zyl, *Introduction To The Physics and Techniques of Remote Sensing*, John Wiley and Sons, 2006.
- 647 [40] A. Marino and N. Walker, "Ship detection in variable sea states and depolarised sea clutter: a polarimetric notch  
648 filter," *Proceeding on POLinSAR*, 2011.
- 649 [41] A. M. Guarnieri, "Adaptive removal of azimuth ambiguities in SAR images," *IEEE Transactions on Geoscience and*  
650 *Remote Sensing*, vol. 43, 2005.
- 651 [42] S. I. Hwang, *A study on ship detection using synthetic aperture radar (in Japanese)*, Ph.D. thesis, National Defense  
652 Academ, Department of Information Science, 2010.
- 653 [43] E. S. Won, K. Ouchi, and C. S. Yang, "Extraction of underwater laver cultivation nets by SAR polarimetric entropy,"  
654 *IEEE Geoscience and Remote Sensing Letters*, vol. 10 (2), pp. 231–235, 2013.
- 655 [44] A. Marino, I. Hajnsek, and N. Walker, "Validating a ship detector based on the notch filter with radarsat-2 fine  
656 quad-pol data," *Proceedings on SEASAR, Tromso, Norway*, 2012.